ACS APPLIED MATERIALS & INTERFACES

Research Article

www.acsami.org

Formation of Carbon Nanosheets via Simultaneous Activation and Catalytic Carbonization of Macroporous Anion-Exchange Resin for Supercapacitors Application

Hui Peng,[†] Guofu Ma,*[,†] Kanjun Sun,[‡] Jingjing Mu,[†] Zhe Zhang,[†] and Ziqiang Lei*[,†]

[†]Key Laboratory of Eco-Environment-Related Polymer Materials of Ministry of Education, Key Laboratory of Polymer Materials of Gansu Province, College of Chemistry and Chemical Engineering, Northwest Normal University, Lanzhou 730070, China

[‡]College of Chemistry and Environmental Science, Lanzhou City University, Lanzhou 730070, China

Supporting Information

ABSTRACT: Two-dimensional mesoporous carbon nanosheets (CNSs) have been prepared via simultaneous activation and catalytic carbonization route using macroporous anion-exchange resin (AER) as carbon precursor and $ZnCl_2$ and $FeCl_3$ as activating agent and catalyst, respectively. The iron catalyst in the skeleton of the AER may lead to carburization to form a sheetlike structure during the carbonization process. The obtained CNSs have a large number of mesopores, a maximum specific surface area of 1764.9 $m^2\ g^{-1}$, and large pore volume of 1.38 $cm^3\ g^{-1}$. As an electrode material for supercapacitors application, the CNSs electrode possesses a large specific capacitance of 283 F g^{-1} at 0.5 A g^{-1} and excellent rate capability (64% retention ratio even at 50 A g^{-1}) in 6 mol L^{-1} KOH. Furthermore, CNSs symmetric supercapacitor exhibits specific energies of 17.2 W h kg^{-1} at a power density of 224 W kg^{-1} operated in the voltage range of 0−1.8 V in 0.5 mol L^{-1} Na_2SO_4 aqueous electrolyte, and outstanding cyclability (retains about 96% initial capacitance after 5000 cycles).

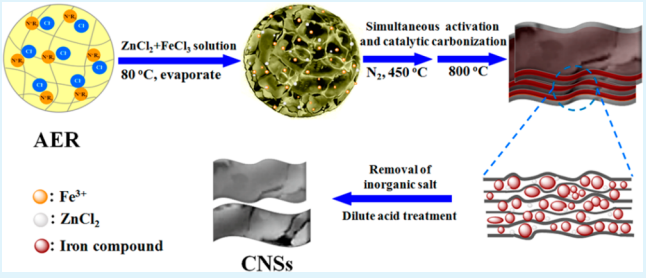

KEYWORDS: *carbon nanosheets, anion-exchange resin, activation, catalytic carbonization, supercapacitors*

INTRODUCTION

Energy storage devices, especially supercapacitors, have gained extensive attention for next generation energy storage applications due to their long cycling stability, high power density, wide operation temperature range, and high safety.[1] Supercapacitors are categorized into electric double-layer capacitors (EDLCs) that store energy in the double layer by charge accumulationon between the surface of electrodes and the electrolyte, such as carbon materials, and pseudocapacitors that mainly derive their energy storage capacity from reversible faradaic reactions at the surface of active material, such as metal oxides and conductive polymers.[2,3] However, most metal oxide-based pseudocapacitors have a narrow available voltage window where they will not be dissolved.[4,5] Moreover, conductive polymer-based pseudocapacitors usually possess an unsatisfactory cycling stability.[6] Actually, the energy density (E) of a supercapacitor is usually limited to the device capacitance (C) and the available voltage window (V) according to the equation $E = {}^1/_2CV^2$. Therefore, to obtain a large E, both C and V are needed to increase. The operation voltage can effectually increase when an organic electrolyte is used in supercapacitors; nevertheless, their low capacitance and unfriendly electrolyte destroy their entire performance for supercapacitor applications.[7] Moreover, electrode materials with a large surface area and abundant mesopore structure is regarded as the most important factor influencing the specific capacitance. The large surface area is beneficial for accumulating a mass of charges, and mesopore structure is advantageous for the diffusion of ions.[1]

To meet such a demand, two-dimensional (2D) carbon nanostructures, especially 2D porous carbon nanomaterials, have been extensively studied as advanced electrode materials for next-generation energy storage devices, attributed to some of their unique properties, such as high electrical conductivity, large surface area, and porous layered structure.[8−10] In addition, the porous structure in carbon materials would be facilitating electrolyte penetration and shorten the ion diffusion distance.[11] Therefore, the porous carbon electrodes generally exhibit excellent electrochemical performance such as larger specific capacitance and excellent rate capability, and such electrodes generally possess various advanced carbon architectures, including graphene, carbon nanosheets, carbon nanofibers, graphite foams, and so on.[12,13] In recent years, various methods can be used to obtain the 2D carbon materials including template method, molten-salt route, chemical vapor deposition (CVD), mechanical cleavage, chemical exfoliation, ball-milling method, and so on.[9,14−19] Wang et al. have reported that using coal tar pitch as a carbon precursor and mesoporous SiO_2

Received: July 30, 2014
Accepted: November 5, 2014
Published: November 5, 2014

nanosheet as a template to prepare the 2D mesoporous carbon sheetlike framework and the material shows excellent capacitive behavior.[9] Feng et al. synthesized highly ordered pore architecture carbon films by a simple coating-etching approach.[14] Recently, Liu et al. controlled carbonization of glucose in molten metal chloride to prepare carbon nanostructures and graphene via a molten-salt (MS) route.[15] You et al. have reported that synthesis of 3D hierarchically porous carbon-CNT-graphene ternary all-carbon foams through self-assembly of graphene oxide-dispersed pristine carbon nanotubes supported on the sponge.[18] Nevertheless, these methods suffer from more or less disadvantages, such as the experimental process complex, special instruments, and/or rigorous conditions. In addition, the choice of the carbon precursor also is an important factor to the preparation of carbon nanosheets.[20−22] Sevilla and Fuertes presented a template-free one-step heat treatment of potassium citrate procedure for the formation of interconnected porous carbon nanosheets.[20] Wang et al. created unique interconnected partially graphitic carbon nanosheets with high specific surface area from hemp bast fiber.[21] Ding et al. synthesized three-dimensional macroporous interconnected networks of carbon nanosheets from peat moss as precursor through a facile carbonization and activation process.[22] However, it is still highly challenging to synthesize carbon nanosheets with abundant porous structure on a large scale simply by carbonization of low-cost resin or other polymers.

Here, we introduce a simultaneous activation and catalytic carbonization route to prepare 2D mesoporous carbon nanosheets (CNSs) directly using the macroporous anion-exchange resin (AER) as carbon precursor and $ZnCl_2$ and $FeCl_3$ as activating agent and catalyst, respectively. The three-electrode and two-electrode cells are fabricated. The symmetric supercapacitor fabricated with CNSs electrodes exhibits a high-energy density of 17.2 W h kg^{-1} at a power density of 224 kW kg^{-1} operated in the voltage range of 0−1.8 V in 0.5 mol L^{-1} Na_2SO_4 aqueous electrolyte. The carbon nanosheets with high capacitance can be attributed to the large specific surface area and the short ion-transport distance which are benefited by the unique porous nanosheet architectures.

EXPERIMENTAL SECTION

Materials. Anion-exchange resin (AER; 717, granularity: 0.3−1.2 mm, Sinopharm Chemical Reagent Co., Ltd., Shanghai, China), ferric trichloride ($FeCl_3$; Shanghai Chemical Works, Shanghai, China), zinc chloride ($ZnCl_2$, Aladdin Ltd., Shanghai, China). All chemical reagents were in analytical grade.

Synthesis of Carbon Nanosheets (CNSs). In a typical synthesis, the pretreated macroporous strongly basic quaternary ammonium-type polystyrene-type AER was mixed with $ZnCl_2$ (AER/$ZnCl_2$ mass ratio is 1:3) in 50 mL of different concentrations of $FeCl_3$ solution (0−3 M). The carbon precursor underwent evaporation at 80 °C until becoming a viscous solution under stirring, and then the aqueous solution was dried to form a solid powder. The obtained carbon precursor mixtures were first activated at 450 °C for 1 h in a N_2 atmosphere at a heating rate of 5 °C min^{-1}. Finally, the mixtures were increased to the ultimate temperatures of 800 °C for 2 h, respectively, with a heating rate of 5 °C min^{-1} in a slow N_2 flow. After being cooled to room temperature, the carbide samples were then thoroughly washed with HCl solution (2 mol L^{-1}) to remove the inorganic salts and other impurities. Finally, the samples were washed with distilled water until neutral pH and dried at 60 °C in ambient conditions for 24 h. The samples treated with different concentrations of $FeCl_3$ (0, 1, 2, and 3 M) were named as CNSs-0, CNSs-1, CNSs-2, and CNSs-3, respectively.

For comparison purposes, the sample treated with 50 mL of $FeCl_3$ solution (3 M) without $ZnCl_2$ was also synthesized under the same conditions. The resultant sample was labeled as CNSs-c.

Materials Characterization. The morphologies of the CNSs products were examined with field emission scanning electron microscopy (FE-SEM, Ultra Plus, Carl Zeiss) and transmission electron microscopy (TEM, JEM-1200EX, 200 kV). The Brunauer−Emmett−Teller surface area (S_{BET}) of the powders was analyzed using nitrogen adsorption in a Micromeritics ASAP 2020 nitrogen adsorption apparatus (Micromeritics Instrument Corporation, Norcross, GA, U.S.A.); all samples were degassed at 200 °C prior to nitrogen adsorption measurements. X-ray diffraction (XRD) of samples was performed using a Rigaku D/Max-2400 diffractometer with Cu Kα radiation (k = 1.5418 Å) at 40 kV, 100 mA. The 2θ measurement range was from 5° to 80°. Raman spectra were recorded with an inVia Raman spectrometer (Renishaw) with an argon ion laser (λ = 514 nm).

Three-Electrode Cell Fabrication. For a conventional three-electrode system, a 5 mm diameter glassy carbon electrode was used as the working electrode. The working electrodes were fabricated similarly to our previous reported literature.[23] Typically, 4 mg of active material (CNSs) was ultrasonically dispersed in 0.4 mL of 0.25 wt % Nafion (DuPont, Wilimington, DE, U.S.A.) ethanol solution. The uniform suspension of 8 μL was dropped onto the surface of a glassy carbon electrode using a pipet gun and dried at room temperature. The three-electrode system was tested in 6 mol L^{-1} KOH aqueous solutions; carbon rod electrode serves as the counter electrode and Hg/HgO as the reference electrode, respectively.

Two-Electrode Cell Fabrication. The capacitive performance of CNSs-3 was investigated using a two-electrode testing device. The working electrode was prepared by mixing the CNSs-3 with commercial carbon black and polymer binder (polyvinylidene fluoride) (8:1:1) in *N*-methyl-2-pyrrolidone solution until it forms a homogeneous slurry. The slurry was coated on nickel foam with a working area of 1.0 cm^2 and the electrodes were dried at 120 °C in ambient conditions for 12 h, and then weighted and pressed into sheets under 15 MPa. The total mass of each electrode was between 3 and 5 mg and we chose the two electrodes with identical or very close weight for the measurements.

Two as-prepared CNSs-3 electrodes fitted with the separator (thin polypropylene film) and electrolyte solution were symmetrically assembled into sandwich-type cells construction (electrode/separator/electrode). Before being assembled into the supercapacitor configuration, CNSs-3 electrodes and separator were immersed in 0.5 mol L^{-1} Na_2SO_4 electrolytes for 12 h to make aqueous electrolyte solutions homogeneously diffuse into the CNSs-3 electrodes.

Electrochemical Measurements. The electrochemical properties of the samples were evaluated by cyclic voltammetry (CV) and galvanostatic charge/discharge measurements in three-electrode cell and two-electrode configuration using a CHI 660D electrochemical workstation. The cycle-life stability was performed using cycling testing equipment (CT2001A, Wuhan Land Electronic Co. Ltd., China). Electrochemical

Scheme 1. Preparation Process of CNSs

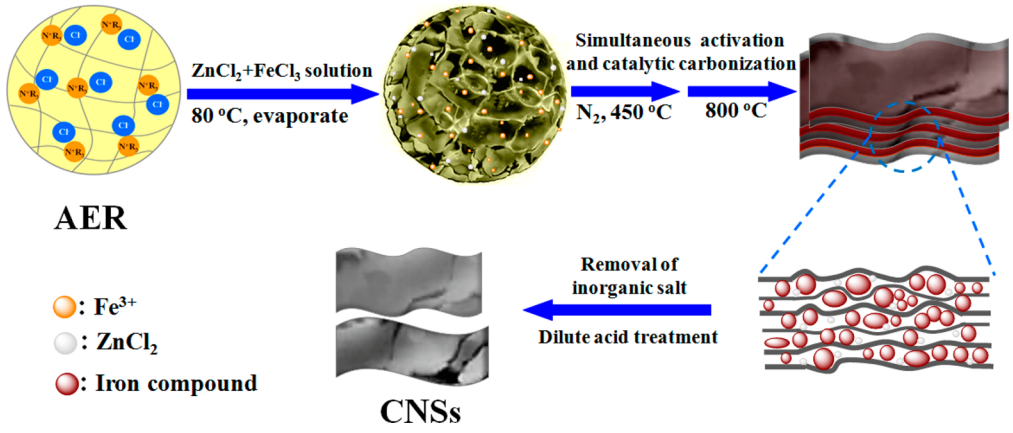

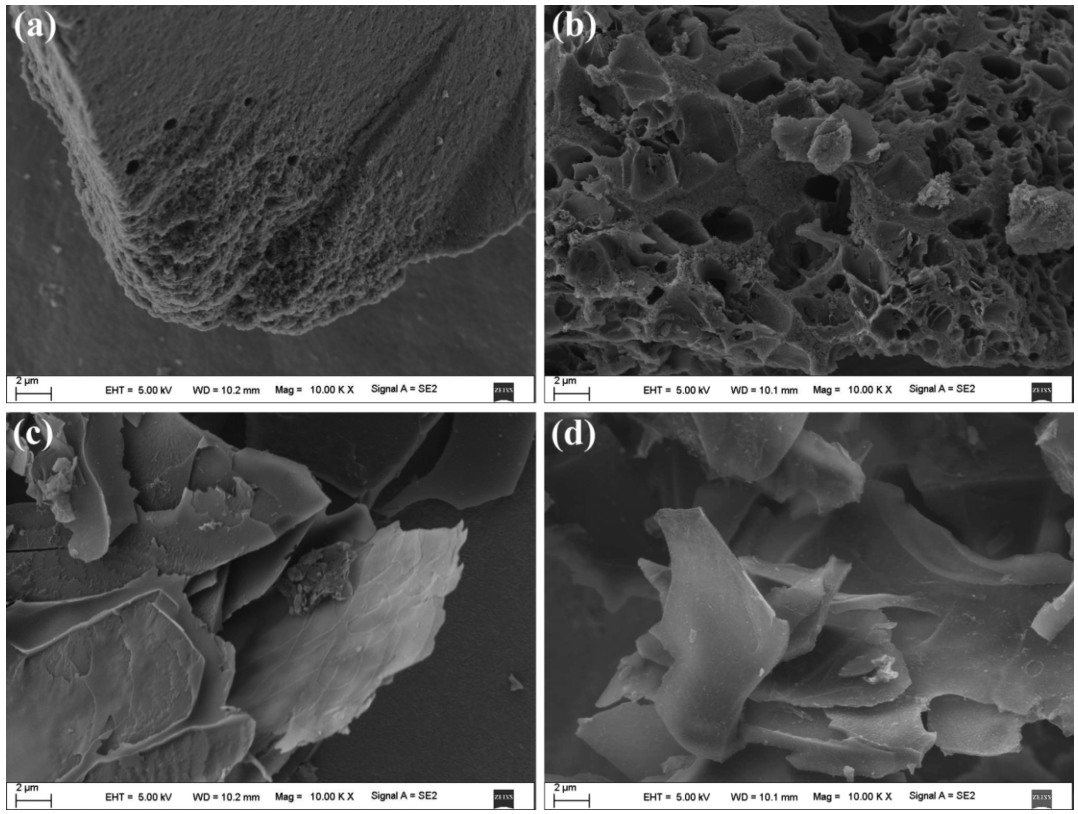

Figure 1. FE-SEM images of CNSs prepared in different concentrations of $FeCl_3$ solution: (a) 0 M; (b) 1 M; (c) 2 M; (d) 3 M.

impedance spectroscopy (EIS) measurements were performed with the Autolab PGSTAT 128N equipped (Eco-chemie, The Netherlands) with FRA module, the frequency ranging from 10 mHz to 100 kHz and an impedance amplitude of ±5 mV at open-circuit potential.

The gravimetric capacitance from galvanostatic charge/discharge was calculated by using the formula of $C_s = 4I\Delta t/(m\Delta V)$ for the two-electrode cells, while, $C_s^* = I\Delta t/(m\Delta V)$ for the three-electrode system, where I is the constant current (A) and m is the mass (g) of electrode material (for the two-electrode cells, m is the total mass of positive and negative electrodes), Δt is the discharge time, and ΔV is the voltage change during the discharge process.

The specific energy density and power density for a supercapacitor cell were defined according to the following equations: $E = {}^1/_2CV^2$ and $P = E/t$, where C is the specific capacitance of the cell, V is the voltage change during the discharge process after the IR drop in galvanostatic discharge curve, t is the corresponding to discharge time, E is the energy density (W h kg^{-1}), and P is the energy density (W kg^{-1}).

RESULTS AND DISCUSSION

Synthesis and Microstructure Characterizations of CNSs. In this work, a new simultaneous activation and catalytic carbonization route is proposed for preparing the mesoporous CNSs. The novel 2D CNSs is designed on the basis of the following: (1) The macroporous strongly basic quaternary ammonium-type polystyrene-type AER is used as carbon precursor, which contains not only a large amount of quaternary ammonium groups ($(CH_3)_3N{-}CH_2{-}$, Scheme 1)

can provide a certain amount of nitrogen source, but also with the special macropore structure can accommodate activating agent and catalyst precursor. (2) $ZnCl_2$ can be added into the skeleton of the macroporous AER and heated to form high surface area and highly porous carbon materials. Meanwhile, the iron catalyst ($FeCl_3$) in the skeleton of the AER may lead to carburization to form a sheetlike structure during the carbonization process.[24] The preparation process of CNSs is shown in Scheme 1. In a typical preparation, AER was mixed with $ZnCl_2$ (mass ratio: 1/3) in 50 mL of different concentrations of $FeCl_3$ solution, after drying the aqueous solution to form a solid powder and then simultaneous activation and catalytic carbonization treated at 800 °C under nitrogen protection. In the process, the iron compound can catalyze carbonization of the AER carbon source lead to the formation of sheetlike structure, and meanwhile, the $ZnCl_2$ activating agent can make the carbon framework to form porous structure. After complete removal of iron nanoparticles and other impurities, the obtained samples were denoted by CNSs-*x* (where *x* is the concentration of $FeCl_3$ solution: 0, 1, 2, and 3 M). We have no further research of the CNSs which were prepared in the concentrations of $FeCl_3$ solution more than 3 M due to the excessive $FeCl_3$ not being able to be completely dissolved.

Figure 1 presents field emission scanning electron microscopy (FE-SEM) images for CNSs prepared in combination with $ZnCl_2$ and different concentrations of $FeCl_3$ solution (0−3 M). When AER is carbonized using only the activating agent $ZnCl_2$, the obtained CNSs-0 displays irregular bulk shape with a rough surface and has no obvious porous structure (Figure 1a). When the activating agent and low concentration of $FeCl_3$ solution (1 M) are incorporated simultaneously into the framework of the macroporous AER, CNSs-1 with abundant and loose macroporous structure can be obtained (Figure 1b). More interestingly, CNSs were prepared by an activating agent and a high concentration of $FeCl_3$ solution (2 and 3 M); the morphology of CNSs-2 and CNSs-3 is present as a sheetlike structure and folded together (Figure 1c,d). Similarly, when AER is carbonized with only $FeCl_3$ catalyst (3 M), the obtained microstructure of CNSs-c displays a stacking sheetlike structure (Figure S1, Supporting Information). These results show that iron catalyst in the skeleton of the AER can play an important role in forming nanosheets-like structure during the simultaneous activation and catalytic carbonization process. The unique structure was further confirmed by TEM (Figure 2). As seen from low-magnification TEM images (Figure 2a,b), CNSs-3 displays a large area of thin sheetlike structure. HRTEM images (Figure 2c,d) of the carbon nanosheets edge shows that the layer architectures of CNSs-3 may present some structural defects and lattice disorder, which would play a significant role in electrolyte ion and charge accommodation region. The inset in Figure 2d is the fast Fourier transform (FFT) of the corresponding HRTEM image. The FFTs displays diffuse spots corresponding to poor crystalline and disordered carbon, which indicates that CNSs exhibiting distorted layers that form the carbon nanosheets. In addition, the multilayer CNSs thickness of about 10 nm is also observed on edge on SEM of CNSs-3, as shown in Figure S2 (Supporting Information).

Nitrogen adsorption−desorption measurement is often used to identify the porosity of the samples. As shown in Figure 3a, all the CNSs exhibited the classical type-IV adsorption−desorption isotherms of mesoporous materials. Moreover, the

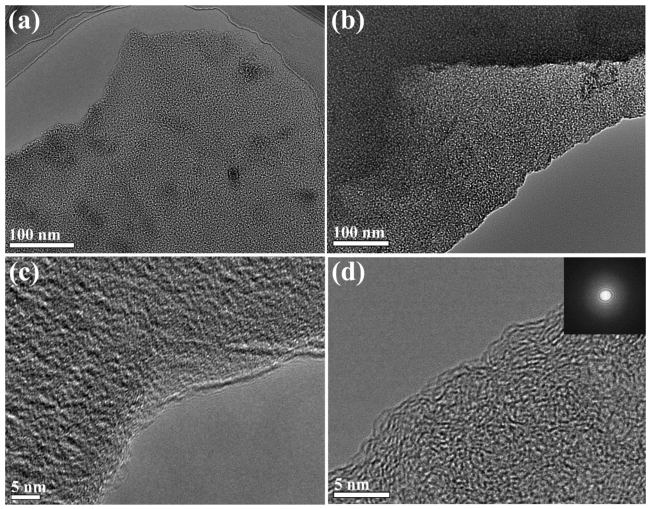

Figure 2. (a,b) TEM images of mesoporous carbon nanosheets (CNSs-3); (c,d) HRTEM images of the carbon nanosheets edge. The inset in (d) is the FFT pattern of the carbon nanosheets.

adsorption−desorption isotherms of the CNSs have a type-H3 hysteresis loop in the relative pressure region between 0.4 and 1.0, which indicates that CNSs have a kind of slit-shaped pore structure. Such slit-shaped pore channels are believed to be constructed from the aggregates or overlap of carbon sheets. In addition, there are also clearly defined step loops at the relative pressures from 0.4 to 0.6, suggesting they possess uniform mesoporous structures.[25] Meanwhile, at low relative pressure, the adsorption isotherms of the samples are rapidly saturated, suggesting the adsorption of micropores. Obviously, as the concentration of $FeCl_3$ solution increases, the adsorbed volume of CNSs increases clearly. Therefore, it is reasonable to conclude that the BET specific surface area increases with increasing the concentration of $FeCl_3$ solution. The corresponding pore size distribution curves of CNSs are shown in Figure 3b, which are calculated using the Barrett−Joyner−Halenda (BJH) model. As the concentration of $FeCl_3$ solution increases, we can observe that the pore sizes of the CNSs-2 and CNSs-3 are distributed narrowly and centered in the range of 2−10 nm, suggesting the existence of abundant mesopores.

The BET surface area and pore structure characterization parameters of CNSs from different concentrations of $FeCl_3$ solution are summarized in Table 1. It is found that the structural character is significantly affected by the concentration of $FeCl_3$ solution. As only the activating agent ($ZnCl_2$) or combination with the low concentration of $FeCl_3$ solution (1 M) are used in the synthesis, both CNSs-0 and CNSs-1 exhibit relatively low surface areas and small pore volumes. Under these synthesis conditions, their pore structure is mainly composed of the micropores or small mesopores. The low adsorption volume and wide pore size distribution of CNSs-0 and CNSs-1 leads to larger average pore size. As the catalyst precursor ($FeCl_3$) concentration increases (CNSs-2 and CNSs-3), both the surface area and the pore volume are enlarged to some extent because of the simultaneous activation and catalytic carbonization process. Obviously, those pores are mainly from the mesoporous pores (>91%, by t-plot method). In particular, the BET surface area and total pore volume of CNSs-3 are 1764.9 $m^2\ g^{-1}$ and 1.38 $cm^3\ g^{-1}$, respectively. However, when AER is carbonized with only $FeCl_3$ catalyst (3 M), the CNSs-c still displays a lower BET surface area (849.7

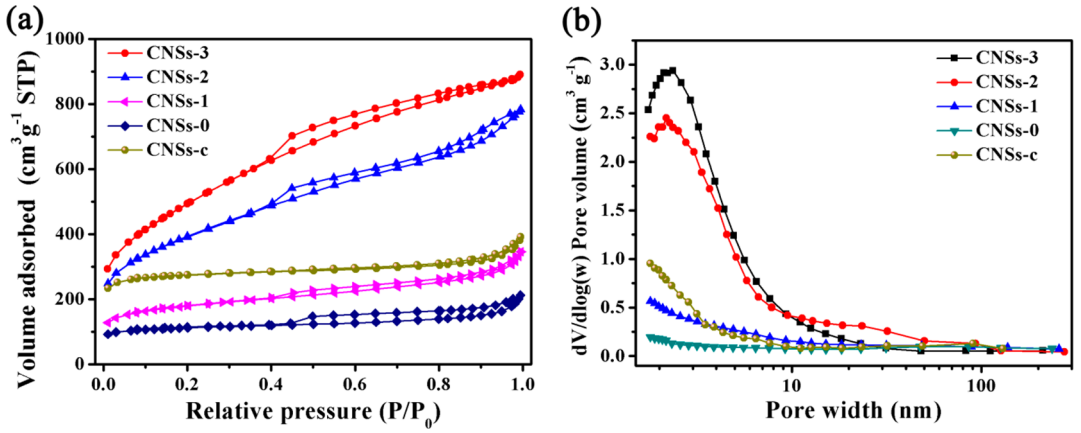

Figure 3. (a) Nitrogen adsorption−desorption isotherms and (b) pore size distribution curves of CNSs prepared in different concentrations of $FeCl_3$ solution.

Table 1. BET Surface Area and Pore Structure Characterization Parameters of CNSs Prepared in Different Concentrations of $FeCl_3$ Solution

samples	methods	S_{BET} [a] (m^2g^{-1})	S_{mjcro} [b] (m^2g^{-1})	pore volume [c] (cm^3g^{-1})	average pore size (nm)
CNSs-0	$ZnCl_2$	352.7	227.8	0.33	3.7
CNSs-1	$ZnCl_2$ + 1 M $FeCl_3$	583.1	233.5	0.56	3.6
CNSs-2	$ZnCl_2$ + 2 M $FeCl_3$	1373.0	124.8	1.21	3.5
CNSs-3	$ZnCl_2$ + 3 M $FeCl_3$	1764.9	102.3	1.38	3.1
CNSs-c	3 M $FeCl_3$	849.7	177.9	0.89	3.3

[a]Specific surface area from multiple BET method. [b]Micropore surface area from t-plot method. [c]Total pore volume at P/P_0 = 0.99.

$m^2\ g^{-1}$) and pore volume (0.89 $cm^3\ g^{-1}$), indicating the need to combine with activating agent ($ZnCl_2$) to increase the BET surface area of the materials. The high specific surface area and extensive pores of CNSs-3 provide abundant ion adsorption sites and a short diffusion path for electrolyte ions. The above results suggest that iron catalyst in the skeleton of the AER can greatly affect the porous structure of carbon materials.

The graphitization degrees of the CNSs can be determined by XRD and Raman spectroscopy analyses. The representative XRD pattern of the CNSs-3 is presented in Figure 4a. Two broad diffraction peaks at about 22.8° and 43.3° are observed, ascribing to the (002) and (100) crystal planes of graphitic carbon, respectively, suggesting that CNSs-3 is made of graphitic carbon and amorphous carbon.[26] Furthermore, the interlayer spacing of CNSs-3 is calculated to be 0.389 nm from the 002 plane, which is slightly larger than that of bulk graphite (0.335 nm). The results can be attributed to stacks of parallel layer planes in different parts increasing the stress in them.[27] The Raman spectrum of the CNSs-3 is shown in Figure 4b. These two prominent peaks at 1330 (D-band) and 1583 cm^{-1} (G-band) are to provide information about the crystallography and structure of the carbon materials. The D-band is associated with disordered carbonaceous structure or graphene edges, while the G-band is attributed to the vibration of all sp^2-hybridized carbon atoms in both rings and chains.[28] Moreover, the D-band peak is weaker than the G-band peak and their intensity ratio (I_D/I_G) is about 0.91, indicating the formation of long-range graphitized carbon with a relatively small number of structural defects.

Electrochemical Behavior of CNSs. The electrochemical properties of the obtained CNSs were first evaluated by a three-electrode system (Figure 5). The cyclic voltammogram (CV) curves of the CNSs prepared in different concentrations of $FeCl_3$ solution (0−3 M) retain quasirectangular shapes at a scan rate of 25 mV s^{-1} in 6.0 M KOH aqueous solution (Figure 5a), which implies that the CNSs materials show the ideal capacitive behavior. For the CNSs-0 and CNSs-1, however, their rectangular CVs are changed to triangular tendency at

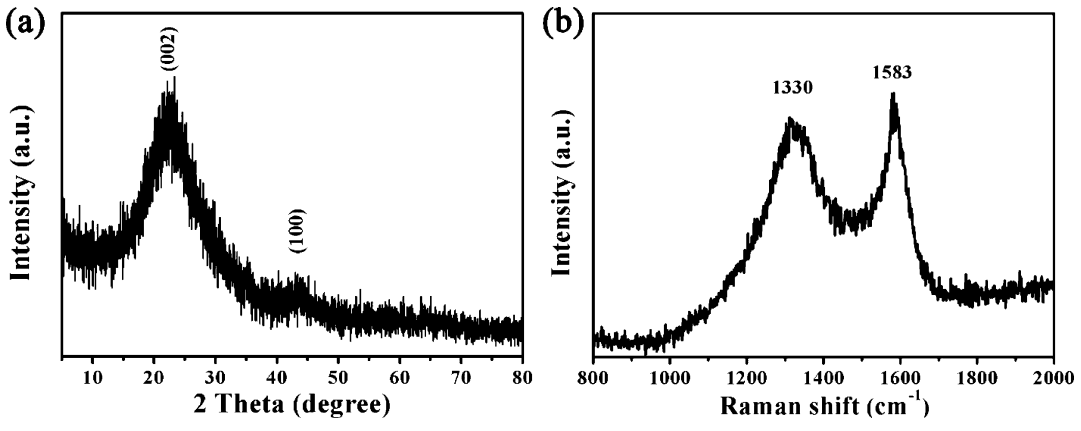

Figure 4. (a) XRD pattern and (b) Raman spectra of CNSs-3.

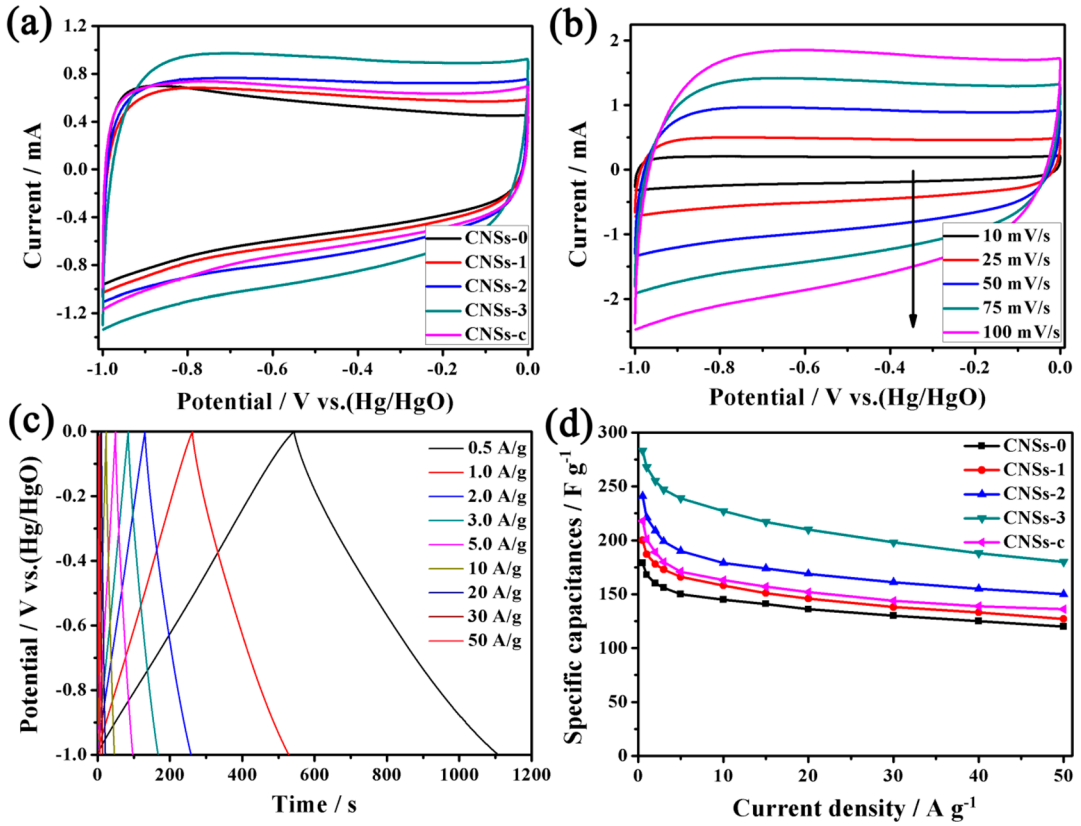

Figure 5. (a) CV curves of CNSs electrodes at a scan rate of 25 mV s^{-1} in 6 M KOH solution; (b) CV curves of CNSs-3 electrode at different scan rates; (c) galvanostatic charge/discharge curves of CNSs-3 electrodes at various current densities; (d) discharge capacitances of CNSs electrodes at various current densities.

high potentials, whose pore dimensions are probably too small to allow ions to diffuse easily and thus lead to an ion sieving effect.[29] Conversely, when the pore size was considerably larger than the ion size, rectangular-shaped CV curves of CNSs-2 and CNSs-3 are obtained. The results also suggest that iron catalyst in the framework of the AER greatly affects the porous structure of CNSs. Obviously, the CNSs-3 has a higher specific capacitance compared to that of other electrodes, due to the linear relation between CV curve area and specific capacitance. In addition, the CV curves of CNSs-3 retain a stable rectangular shape even at a scan rate of up to 100 mV s^{-1} (Figure 5b), suggesting the material exhibits a remarkable high rate capability.

The galvanostatic charge/discharge measurements were further carried out at various current densities ranging from 0.5 to 50 A g^{-1} within the potential window from −1.0 to 0 V to calculate the specific capacitances of the CNSs, and the typical results are shown in Figure 5c. All the curves are highly symmetrical at various current densities, meaning that such electrode possesses excellent electrochemical reversibility and charge/discharge properties. The correlation between the specific capacitance and the various current densities for different electrodes are presented in Figure 5d. As for these porous carbon materials, CNSs-3 exhibits the highest specific capacitance of 283 F g^{-1} at 0.5 A g^{-1}, as compared to 179 F g^{-1} at 0.5 A g^{-1} for porous material prepared using only the $ZnCl_2$ activating agent, 200 and 241 F g^{-1} at 0.5 A g^{-1} for CNSs materials prepared with a combination of the activating agent $ZnCl_2$ and 1 or 2 M $FeCl_3$ solution, respectively. More interestingly, CNSs-3 exhibits a high capacitance retention ratio (64%) at current densities from 0.5 to 50 A g^{-1}. The results indicate a very fast and efficient charge transfer and the high capacitance of CNSs-3 electrode can be maintained under such a high current density. The nanosheets morphology of the obtained carbon materials facilitates the efficient access of electrolytes and shortens the ion transport length, leading to high specific capacitance. Additionally, the CNSs has a certain amount of N-doping content (N content in as-prepared CNSs-3 is around 1.52 wt % by combustion elemental analysis\), which is helpful for enhancing surface wettability and electronic conductivity of electrode materials, and thus improving their electrochemical performance.[30]

The high-performance CNSs electrodes were further examined by the electrochemical impedance spectroscopic (EIS) test in a frequency range from 0.1 Hz to 100 kHz (Figure S3). The Nyquist plots of CNSs materials exhibit an uncompleted semicircle in the high-frequency region, indicating the interfacial charge-transfer resistance of the material. Meanwhile, CNSs-3 and CNSs-2 exhibit small semicircles, which suggests their low interfacial charge-transfer resistances. The equivalent series resistances of all the CNSs materials are around 3 Ω, which is determined from the x intercept of the Nyquist plots (inset in Figure S3). For all CNSs materials, the straight 45° sloped line in the low frequency is the Warburg resistance resulting from the frequency dependence of ion diffusion/transport in the electrolyte. In addition, the Nyquist plots of CNSs-3, CNSs-2, and CNSs-1 show a nearly vertical line at low frequency, indicating the behavior of an ideal capacitor.

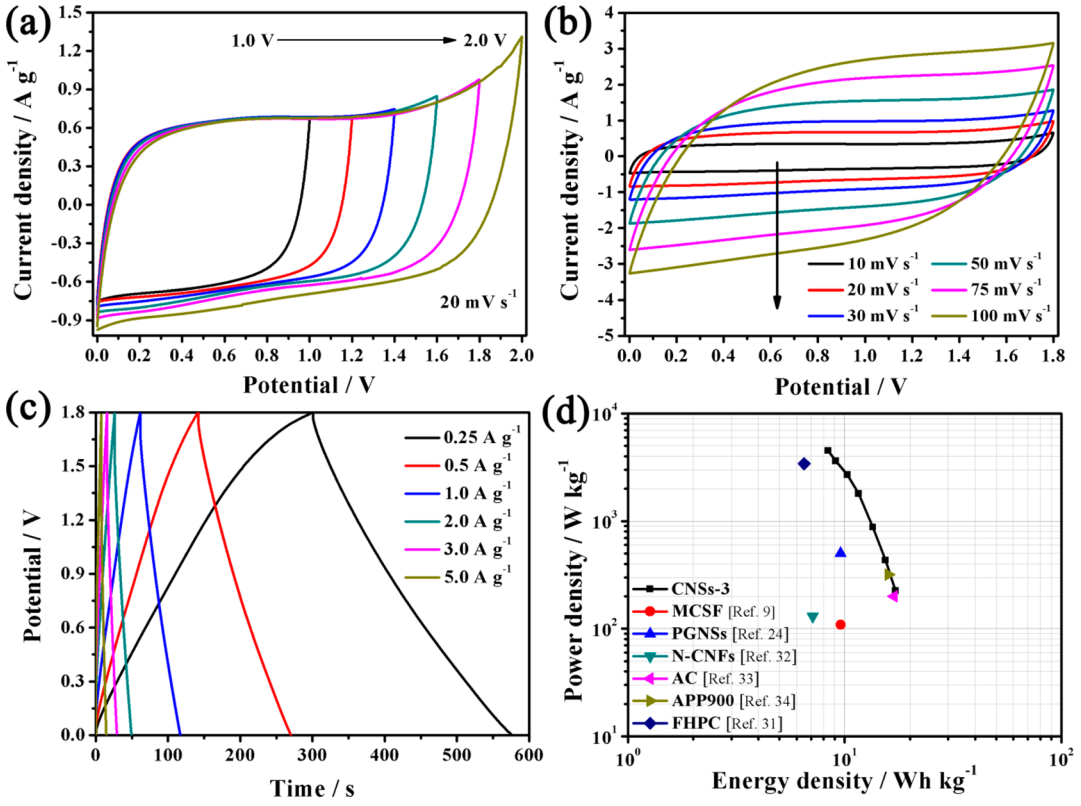

Figure 6. (a) CV curves of the CNSs-3 symmetric two-electrode cell at different voltage windows in 0.5 M Na_2SO_4 aqueous electrolytes; (b) CV curves of the CNSs-3 electrode at various scan rates; (c) galvanostatic charge/discharge curves of CNSs-3//CNSs-3 symmetric cell at various current densities; (d) Ragone plot of the CNSs-3//CNSs-3 symmetric cell in comparison to carbon-based aqueous symmetric cells recently reported in the literature.

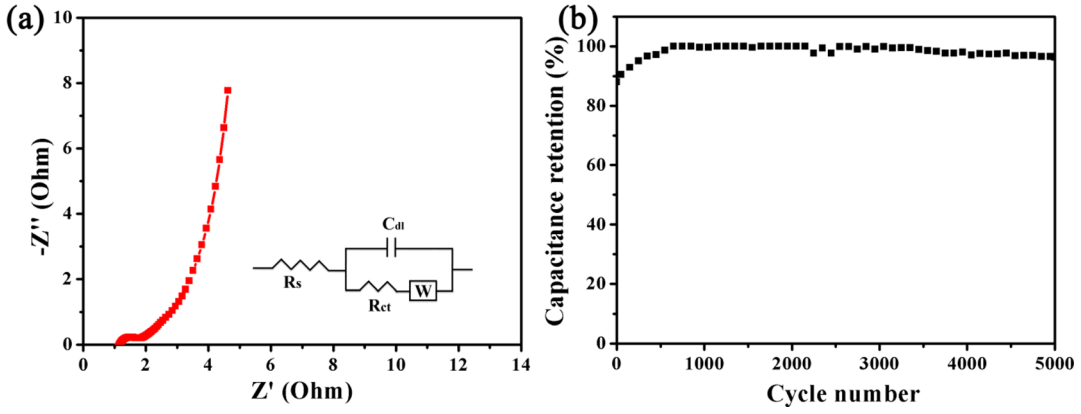

Figure 7. (a) Nyquist plots of two-electrode symmetric cell base on CNSs-3 electrodes and (b) cycling stability of CNSs-3 symmetric cell.

To further estimate the actual electrochemical performance of CNSs-3, we have also fabricated the symmetric two-electrode cell. It is reported that the neutral Na_2SO_4 aqueous electrolyte possesses a higher operation voltage than that of acid and alkali solutions.[31] Therefore, the CNSs-3 symmetric supercapacitor was assembled and characterized in 0.5 M Na_2SO_4 aqueous electrolyte. The as-assembled symmetric cell was first measured at different potential windows at a scan rate of 20 mV s^{-1} (Figure 6a). The CV curves of the supercapacitor are rectangular-like shape even when the high voltage extends to 1.8 V, indicating ideal capacitive behavior and good reversibility. When the operating voltage increases to 2.0 V, however, the current is sharply increased since the electrolyte could be decomposed to hydrogen and/or oxygen. Therefore, the wide potential window of 1.8 V is chosen to further estimate the electrochemical performance of the symmetric cell.

Figure 6b shows the typical CV curves at different scan rates from 10 to 100 mV s^{-1}. We can see that the CNSs-3//CNSs-3 symmetric cell devices can still keep a quasirectangular shape even at a scan rate of 100 mV s^{-1}. Typical galvanostatic charge/discharge curves of the electrode at different current densities from 0.25 to 5 A g^{-1} are displayed in Figure 6c. It can be seen that all the galvanostatic charge/discharge curves are close to the typical isosceles triangle and the charge and discharge curves are symmetric. These results indicate that the symmetric cell possesses ideal capacitive behaviors and excellent electrochemical reversibility.

dx.doi.org/10.1021/am505066v | ACS Appl. Mater. Interfaces 2014, 6, 20795−20803

The Ragone plot related to specific energy and power densities of the CNSs-3//CNSs-3 symmetric two-electrode systems is estimated from galvanostatic discharge curves at the different currents, as shown in Figure 6d. The CNSs-3//CNSs-3 symmetric cell shows the highest energy density is 17.2 W h kg^{1-} at a power density of 224 W kg^{1-} and even remained at 8.4 W h kg^{1-} at a power density of 4500 W kg^{1-}, revealing that the specific energy of electrode material decreases with increasing specific power. Furthermore, the obtained maximum energy density is considerably higher than those previously reported carbon-based aqueous symmetric cells.[9,24,31−34] We also compared with symmetric cells (list there are electrolyte, operation voltage, and energy-power values) used various carbon materials previously reported in the literature, as listed in Table S1 (Supporting Information).

Figure 7a shows the Nyquist plot of the two-electrode symmetric cell base on CNSs-3 electrodes and the equivalent circuit for the fitting of the EIS data achieved by ZSimpWin software (the inset). In the high-frequency region, the imaginary part (Z′) of the impedance is very small and the real part of resistance (Z″) corresponds to the ohmic resistance derived from the electrolyte and the contact between the current collector and the active material (R_s). An uncompleted semicircle loop in the medium-high frequencies region can be observed, which stands for charge-transfer resistance (R_{ct}) caused by Faradaic reactions and electronic double-layer capacitor (C_{dl}) at the interface between the electrode and electrolyte.[35] The inclined portion of the curve (about 45°) in the middle frequencies is called the Warburg impedance (W) and is a result of the frequency dependence of ion diffusion/transport in electrolyte.[36] In the low-frequency region, the greater than 45° vertical curve represents the ideal capacitive behavior of the carbon material.[37] As shown in Figure 7a, the internal resistance of CNSs-3 is 1.07 Ω, indicating high electrical conductivity of the test symmetric cell. Figure 7b displays the capacitance retentions versus cycle number curves of CNSs-3 at a current density of 5 A g^{-1} for 5000 cycles. As can be seen, the specific capacitance increases slightly before the initial 800 cycles and then decreases slightly and remains at about 96% of the initial capacitance after 5000 cycles, meaning that the electrode has stable energy-storage processes and a high degree of electrochemical reversibility. The increased capacitance during the initial 800 cycles may be due to the improvement of surface wetting between the electrode and the electrolyte during long a cycle charge/discharge process.[11]

CONCLUSIONS

In summary, the mesoporous carbon nanosheets were successfully prepared by simultaneous activation and catalytic carbonization of macroporous AER. In this process, the activating agent ($ZnCl_2$) and catalyst precursor ($FeCl_3$) in the skeleton of the AER could make simultaneous realization of activation and catalyst carbonization for enhancing formation of the carbon nanosheets. The mesoporous carbon nanosheets possess excellent capacitive performance as electrodes of supercapacitors, which are mainly attributed to the unique nanosheets morphology and the abundant mesoporous structure. The present method can be further extended to fabricate a variety of graphitized mesoporous carbon nanosheets with high specific surface area and large pore volume using other polymer-based carbon precursors.

ASSOCIATED CONTENT

Supporting Information

FE-SEM images of CNSs-c prepared in carbonized AER with only $FeCl_3$ catalyst. Edge on SEM of CNSs-3 to measure the carbon nanosheet thickness. Nyquist plots of CNSs electrodes. Performances comparison of symmetric cells used various carbon materials in the references. This material is available free of charge via the Internet at http://pubs.acs.org/.

AUTHOR INFORMATION

Corresponding Authors

*E-mail: magf@nwnu.edu.cn (G. Ma).
*E-mail: Leizq@nwnu.edu.cn (Z. Lei).

Notes

The authors declare no competing financial interest.

ACKNOWLEDGMENTS

The research was financially supported by the National Science Foundation of China (No. 21164009, 21174114), the program for Changjiang Scholars and Innovative Research Team in University (IRT1177), the Science and Technology Program of Gansu Province (No. 1308RJZA295, 1308RJZA265), Key Laboratory of Eco-Environment-Related Polymer Materials (Northwest Normal University) of Ministry of Education, and Key Laboratory of Polymer Materials of Gansu Province.

REFERENCES

(1) Zhang, L.; Zhao, X. Carbon-Based Materials as Supercapacitor Electrodes. *Chem. Soc. Rev.* **2009**, *38*, 2520−2531.
(2) Conway, B. E. *Electrochemical Supercapacitors: Scientific Fundamentals and Technological Applications*, 1st ed; Kluwar Academic: New York, 1999.
(3) Jiang, H.; Lee, P. S.; Li, C. 3D Carbon Based Nanostructures for Advanced Supercapacitors. *Energy Environ. Sci.* **2013**, *6*, 41−53.
(4) Wang, H.; Casalongue, H. S.; Liang, Y.; Dai, H. $Ni(OH)_2$ Nanoplates Grown on Graphene as Advanced Electrochemical Pseudocapacitor Materials. *J. Am. Chem. Soc.* **2010**, *132*, 7472−7477.
(5) Li, Z.; Xu, Z.; Wang, H.; Ding, J.; Zahiri, B.; Holt, C. M. B.; Tan, X.; Mitlin, D. Colossal Pseudocapacitance in a High Functionality-High Surface Area Carbon Anode Doubles the Energy of an Asymmetric Supercapacitor. *Energy Environ. Sci.* **2014**, *7*, 1708−1718.
(6) Snook, G. A.; Kao, P.; Best, A. S. Conducting-Polymer-Based Supercapacitor Devices and Electrodes. *J. Power Sources* **2011**, *196*, 1−12.
(7) Chang, J.; Jin, M.; Yao, F.; Kim, T. H.; Le, V. T.; Yue, H.; Gunes, F.; Li, B.; Ghosh, A.; Xie, S.; Lee, Y. H. Asymmetric Supercapacitors Based on Graphene/MnO_2 Nanospheres and Graphene/MoO_3 Nanosheets with High Energy Density. *Adv. Funct. Mater.* **2013**, *23*, 5074−5083.
(8) Luo, G.; Liu, L.; Zhang, J.; Li, G.; Wang, B.; Zhao, J. Hole Defects and Nitrogen Doping in Graphene: Implication for Supercapacitor Applications. *ACS Appl. Mater. Interfaces* **2013**, *5*, 11184−11193.
(9) Wang, Q.; Yan, J.; Wei, T.; Feng, J.; Ren, Y.; Fan, Z.; Zhang, M.; Jing, X. Two-Dimensional Mesoporous Carbon Sheet-Like Framework Material for High-Rate Supercapacitors. *Carbon* **2013**, *60*, 481−487.
(10) Wang, H.; Wu, Z.; Meng, F.; Ma, D.; Huang, X.; Wang, L.; Zhang, X. Nitrogen-Doped Porous Carbon Nanosheets as Low-Cost, High-Performance Anode Material for Sodium-Ion Batteries. *ChemSusChem* **2013**, *6*, 56−60.
(11) Fan, Z.; Liu, Y.; Yan, J.; Ning, G.; Wang, Q.; Wei, T.; Zhi, L.; Wei, F. Template-Directed Synthesis of Pillared-Porous Carbon Nanosheet Architectures: High-Performance Electrode Materials for Supercapacitors. *Adv. Energy Mater.* **2012**, *2*, 419−424.
(12) Zhai, Y.; Dou, Y.; Zhao, D.; Fulvio, P. F.; Mayes, R. T.; Dai, S. Carbon Materials for Chemical Capacitive Energy Storage. *Adv. Mater.* **2011**, *23*, 4828−4850.

(13) Xia, X.; Chao, D.; Fan, Z.; Guan, C.; Cao, X.; Zhang, H.; Fan, H. J. A New Type of Porous Graphite Foams and Their Integrated Composites with Oxide/Polymer Core/Shell Nanowires for Supercapacitors: Structural Design, Fabrication, and Full Supercapacitor Demonstrations. *Nano Lett.* **2014**, *14*, 1651−1658.
(14) Feng, D.; Lv, Y.; Wu, Z.; Dou, Y.; Han; Sun, Z.; Xia, Y.; Zheng, G.; Zhao, D. Free-Standing Mesoporous Carbon Thin Films with Highly Ordered Pore Architectures for Nanodevices. *J. Am. Chem. Soc.* **2011**, *133*, 15148−15156.
(15) Liu, X.; Giordano, C.; Antonietti, M. A Facile Molten-Salt Route to Graphene Synthesis. *Small* **2014**, *10*, 193−200.
(16) Liu, W.; Dang, T.; Xiao, Z.; Li, X.; Zhu, C.; Wang, X. Carbon Nanosheets with Catalyst-Induced Wrinkles Formed by Plasma-Enhanced Chemical-Vapor Deposition. *Carbon* **2011**, *49*, 884−889.
(17) Jeon, I. Y.; Choi, H. J.; Jung, S. M.; Seo, J. M.; Kim, M. J.; Dai, L.; Baek, J. B. Large-Scale Production of Edge-Selectively Functionalized Graphene Nanoplatelets via Ball Milling and Their Use as Metal-Free Electrocatalysts for Oxygen Reduction Reaction. *J. Am. Chem. Soc.* **2013**, *135*, 1386−1393.
(18) You, B.; Jiang, J.; Fan, S. Three-Dimensional Hierarchically Porous All-Carbon Foams for Supercapacitor. *ACS Appl. Mater. Interfaces* **2014**, *6*, 15302−15308.
(19) Lu, H.; Boulos, R. A.; Chan, B. C. Y.; Gibson, C. T.; Wang, X.; Raston, C. L.; Chu, H. Carbon Nanofibres from Fructose using a Light-driven High-Temperature Spinning Disc Processor. *Chem. Commun.* **2014**, *50*, 1478−1480.
(20) Sevilla, M.; Fuertes, A. B. Direct Synthesis of Highly Porous Interconnected Carbon Nanosheets and Their Application as High-Performance Supercapacitors. *ACS Nano* **2014**, *8*, 5069−5078.
(21) Wang, H.; Xu, Z.; Kohandehghan, A.; Li, Z.; Cui, K.; Tan, X.; Stephenson, T. J.; King'ondu, C. K.; Holt, C. M. B.; Olsen, B. C.; Tak, J. K.; Harfield, D.; Anyia, A. O.; Mitlin, D. Interconnected Carbon Nanosheets Derived from Hemp for Ultrafast Supercapacitors with High Energy. *ACS Nano* **2013**, *7*, 5131−5141.
(22) Ding, J.; Wang, H.; Li, Z.; Kohandehghan, A.; Cui, K.; Xu, Z.; Zahiri, B.; Tan, X.; Lotfabad, E. M.; Olsen, B. C.; Mitlin, D. Carbon Nanosheet Frameworks Derived from Peat Moss as High Performance Sodium Ion Battery Anodes. *ACS Nano* **2013**, *7*, 11004−11015.
(23) Peng, H.; Ma, G.; Mu, J.; Sun, K.; Lei, Z. Low-Cost and High Energy Density Asymmetric Supercapacitors Based on Polyaniline Nanotubes and MoO_3 Nanobelts. *J. Mater. Chem. A* **2014**, *2*, 10384−10388.
(24) Sun, L.; Tian, C.; Li, M.; Meng, X.; Wang, L.; Wang, R.; Yin, J.; Fu, H. From Coconut Shell to Porous Graphene-Like Nanosheets for High-Power Supercapacitors. *J. Mater. Chem. A* **2013**, *1*, 6462−6470.
(25) He, Q.; Ma, M.; Wei, C.; Shi, J. Mesoporous Carbon@Silicon-Silica Nanotheranostics for Synchronous Delivery of Insoluble Drugs and Luminescence Imaging. *Biomaterials* **2012**, *33*, 4392−4402.
(26) Su, P.; Jiang, L.; Zhao, J.; Yan, J.; Li, C.; Yang, Q. Mesoporous Graphitic Carbon Nanodisks Fabricated via Catalytic Carbonization of Coordination Polymers. *Chem. Commun.* **2012**, *48*, 8769−8771.
(27) Kuang, Q.; Xie, S.; Jiang, Z.; Zhang, X.; Xie, Z.; Huang, R.; Zheng, L. Low Temperature Solvothermal Synthesis of Crumpled Carbon Nanosheets. *Carbon* **2004**, *42*, 1737−1741.
(28) Dresselhaus, M. S.; Jorio, A.; Hofmann, M.; Dresselhaus, G.; Saito, R. Perspectives on Carbon Nanotubes and Graphene Raman Spectroscopy. *Nano Lett.* **2010**, *10*, 751−758.
(29) Eliad, L.; Salitra, G.; Soffer, A.; Aurbach, D. Ion Sieving Effects in the Electrical Double Layer of Porous Carbon Electrodes: Estimating Effective Ion Size in Electrolytic Solutions. *J. Phys. Chem. B* **2001**, *105*, 6880−6887.
(30) Wu, Z.; Yang, S.; Sun, Y.; Parvez, K.; Feng, X.; Müllen, K. 3D Nitrogen-Doped Graphene Aerogel-Supported Fe_3O_4 Nanoparticles as Efficient Electrocatalysts for the Oxygen Reduction Reaction. *J. Am. Chem. Soc.* **2012**, *134*, 9082−9085.
(31) Wang, Q.; Yan, J.; Wang, Y.; Wei, T.; Zhang, M.; Jing, X.; Fan, Z. Three-Dimensional Flower-Like and Hierarchical Porous Carbon Materials as High-Rate Performance Electrodes for Supercapacitors. *Carbon* **2014**, *67*, 119−127.
(32) Chen, L.; Zhang, X.; Liang, H.; Kong, M.; Guan, Q.; Chen, P.; Wu, Z.; Yu, S. Synthesis of Nitrogen-Doped Porous Carbon Nanofibers as an Efficient Electrode Material for Supercapacitors. *ACS Nano* **2012**, *6*, 7092−7102.
(33) Sun, X.; Zhang, X.; Zhang, H.; Zhang, D.; Ma, Y. A Comparative Study of Activated Carbon-Based Symmetric Supercapacitors in Li_2SO_4 and KOH Aqueous Electrolytes. *J. Solid State Electrochem.* **2012**, *16*, 2597−2603.
(34) Huang, C.; Puziy, A. M.; Sun, T.; Poddubnaya, O. I.; Suárez-García, F.; Tascón, J. M. D.; Hulicova-Jurcakova, D. Capacitive Behaviours of Phosphorus-Rich Carbons Derived from Lignocelluloses. *Electrochim. Acta* **2014**, *137*, 219−227.
(35) Hu, C.; Chu, C. Electrochemical Impedance Characterization of Polyaniline-Coated Graphite Electrodes for Electrochemical Capacitors-Effects of Film Coverage/Thickness and Anions. *J. Electroanal. Chem.* **2001**, *503*, 105−116.
(36) Zhang, D.; Zhang, X.; Chen, Y.; Yu, P.; Wang, C.; Ma, Y. Enhanced Capacitance and Rate Capability of Graphene/Polypyrrole Composite as Electrode Material for Supercapacitors. *J. Power Sources* **2011**, *196*, 5990−5996.
(37) Yan, J.; Wei, T.; Shao, B.; Ma, F.; Fan, Z.; Zhang, M.; Zheng, C.; Shang, Y.; Qian, W.; Wei, F. Electrochemical Properties of Graphene Nanosheet/Carbon Black Composites as Electrodes for Supercapacitors. *Carbon* **2010**, *48*, 1731−1737.